



# Common-path phase-sensitive optical coherence tomography provides enhanced phase stability and detection sensitivity for dynamic elastography

GONGPU LAN,<sup>1</sup> MANMOHAN SINGH,<sup>2</sup> KIRILL V. LARIN,<sup>2,3</sup> AND MICHAEL D. TWA<sup>1,\*</sup>

<sup>1</sup>*School of Optometry, University of Alabama at Birmingham, Birmingham, AL, USA*

<sup>2</sup>*Biomedical Engineering, University of Houston, Houston, TX, USA*

<sup>3</sup>*Interdisciplinary Laboratory of Biophotonics, Tomsk State University, Tomsk, Russia*

\*[mtwa@uab.edu](mailto:mtwa@uab.edu)

**Abstract:** Phase-sensitive optical coherence elastography (PhS-OCE) is an emerging optical technique to quantify soft-tissue biomechanical properties. We implemented a common-path OCT design to enhance displacement sensitivity and optical phase stability for dynamic elastography imaging. The background phase stability was greater in common-path PhS-OCE ( $0.24 \pm 0.07\text{nm}$ ) than conventional PhS-OCE ( $1.60 \pm 0.11\mu\text{m}$ ). The coefficient of variation for surface displacement measurements using conventional PhS-OCE averaged 11% versus 2% for common-path PhS-OCE. Young's modulus estimates showed good precision (95% CIs) for tissue phantoms:  $24.96 \pm 2.18\text{kPa}$  (1% agar),  $49.69 \pm 4.87\text{kPa}$  (1.5% agar), and  $116.08 \pm 12.14\text{kPa}$  (2% agar), respectively. Common-path PhS-OCE effectively reduced the amplitude of background dynamic optical phase instability to a sub-nanometer level, which provided a larger dynamic detection range and higher detection sensitivity for surface displacement measurements than conventional PhS-OCE.

© 2017 Optical Society of America under the terms of the [OSA Open Access Publishing Agreement](#)

**OCIS codes:** (110.4500) Optical coherence tomography; (120.5050) Phase measurement; (120.4570) Optical design of instruments; (170.3880) Medical and biological imaging; (120.7280) Vibration analysis; Elastography.

## References and links

1. J. F. Greenleaf, M. Fatemi, and M. Insana, "Selected methods for imaging elastic properties of biological tissues," *Annu. Rev. Biomed. Eng.* **5**, 57–78 (2003).
2. A. Sarvazyan, T. J. Hall, M. W. Urban, M. Fatemi, S. R. Aglyamov, and B. S. Garra, "An Overview of Elastography - an Emerging Branch of Medical Imaging," *Curr. Med. Imaging Rev.* **7**(4), 255–282 (2011).
3. S. Wang and K. V. Larin, "Optical coherence elastography for tissue characterization: a review," *J. Biophotonics* **8**(4), 279–302 (2015).
4. K. V. Larin and D. D. Sampson, "Optical coherence elastography - OCT at work in tissue biomechanics," *Biomed. Opt. Express* **8**(2), 1172–1202 (2017).
5. J. Schmitt, "OCT elastography: imaging microscopic deformation and strain of tissue," *Opt. Express* **3**(6), 199–211 (1998).
6. J. Ophir, I. Céspedes, H. Ponnekanti, Y. Yazdi, and X. Li, "Elastography: a quantitative method for imaging the elasticity of biological tissues," *Ultrason. Imaging* **13**(2), 111–134 (1991).
7. C. L. de Korte, A. F. van der Steen, E. I. Céspedes, and G. Pasterkamp, "Intravascular ultrasound elastography in human arteries: initial experience in vitro," *Ultrasound Med. Biol.* **24**(3), 401–408 (1998).
8. K. Nightingale, S. McAleavey, and G. Trahey, "Shear-wave generation using acoustic radiation force: in vivo and ex vivo results," *Ultrasound Med. Biol.* **29**(12), 1715–1723 (2003).
9. R. Muthupillai, D. J. Lomas, P. J. Rossman, J. F. Greenleaf, A. Manduca, and R. L. Ehman, "Magnetic resonance elastography by direct visualization of propagating acoustic strain waves," *Science* **269**(5232), 1854–1857 (1995).
10. A. Manduca, T. E. Oliphant, M. A. Dresner, J. L. Mahowald, S. A. Kruse, E. Amromin, J. P. Felmlee, J. F. Greenleaf, and R. L. Ehman, "Magnetic resonance elastography: non-invasive mapping of tissue elasticity," *Med. Image Anal.* **5**(4), 237–254 (2001).
11. D. Huang, E. A. Swanson, C. P. Lin, J. S. Schuman, W. G. Stinson, W. Chang, M. R. Hee, T. Flotte, K. Gregory, C. A. Puliafito, *et al.*, "Optical coherence tomography," *Science* **254**(5035), 1178–1181 (1991).

12. Y. Zhao, Z. Chen, C. Saxer, S. Xiang, J. F. de Boer, and J. S. Nelson, "Phase-resolved optical coherence tomography and optical Doppler tomography for imaging blood flow in human skin with fast scanning speed and high velocity sensitivity," *Opt. Lett.* **25**(2), 114–116 (2000).
13. S. J. Kirkpatrick, R. K. Wang, and D. D. Duncan, "OCT-based elastography for large and small deformations," *Opt. Express* **14**(24), 11585–11597 (2006).
14. R. K. K. Wang, Z. H. Ma, and S. J. Kirkpatrick, "Tissue Doppler optical coherence elastography for real time strain rate and strain mapping of soft tissue," *Appl. Phys. Lett.* **89**, 144103 (2006).
15. R. K. Wang and A. L. Nuttall, "Phase-sensitive optical coherence tomography imaging of the tissue motion within the organ of Corti at a subnanometer scale: a preliminary study," *J. Biomed. Opt.* **15**(5), 056005 (2010).
16. M. H. De la Torre-Ibarra, P. D. Ruiz, and J. M. Huntley, "Double-shot depth-resolved displacement field measurement using phase-contrast spectral optical coherence tomography," *Opt. Express* **14**(21), 9643–9656 (2006).
17. M. Sticker, C. K. Hitznerberger, R. Leitgeb, and A. F. Fercher, "Quantitative differential phase measurement and imaging in transparent and turbid media by optical coherence tomography," *Opt. Lett.* **26**(8), 518–520 (2001).
18. M. D. Twa, J. Li, S. Vantipalli, M. Singh, S. Aglyamov, S. Emelianov, and K. V. Larin, "Spatial characterization of corneal biomechanical properties with optical coherence elastography after UV cross-linking," *Biomed. Opt. Express* **5**(5), 1419–1427 (2014).
19. J. Li, S. Wang, R. K. Manapuram, M. Singh, F. M. Menodiado, S. Aglyamov, S. Emelianov, M. D. Twa, and K. V. Larin, "Dynamic optical coherence tomography measurements of elastic wave propagation in tissue-mimicking phantoms and mouse cornea in vivo," *J. Biomed. Opt.* **18**(12), 121503 (2013).
20. S. Song, Z. Huang, and R. K. Wang, "Tracking mechanical wave propagation within tissue using phase-sensitive optical coherence tomography: motion artifact and its compensation," *J. Biomed. Opt.* **18**(12), 121505 (2013).
21. J. Zhu, Y. Qu, T. Ma, R. Li, Y. Du, S. Huang, K. K. Shung, Q. Zhou, and Z. Chen, "Imaging and characterizing shear wave and shear modulus under orthogonal acoustic radiation force excitation using OCT Doppler variance method," *Opt. Lett.* **40**(9), 2099–2102 (2015).
22. S. Song, W. Wei, B. Y. Hsieh, I. Pelivanov, T. T. Shen, M. O'Donnell, and R. K. Wang, "Strategies to improve phase-stability of ultrafast swept source optical coherence tomography for single shot imaging of transient mechanical waves at 16 kHz frame rate," *Appl. Phys. Lett.* **108**(19), 191104 (2016).
23. S. Song, Z. Huang, T.-M. Nguyen, E. Y. Wong, B. Arnal, M. O'Donnell, and R. K. Wang, "Shear modulus imaging by direct visualization of propagating shear waves with phase-sensitive optical coherence tomography," *J. Biomed. Opt.* **18**(12), 121509 (2013).
24. M. P. Norton and D. G. Karczub, *Fundamentals of Noise and Vibration Analysis for Engineers* (Cambridge University Press, 2003).
25. S. H. Yun, G. Tearney, J. de Boer, and B. Bouma, "Motion artifacts in optical coherence tomography with frequency-domain ranging," *Opt. Express* **12**(13), 2977–2998 (2004).
26. B. I. Akca, E. W. Chang, S. Kling, A. Ramier, G. Scarcelli, S. Marcos, and S. H. Yun, "Observation of sound-induced corneal vibrational modes by optical coherence tomography," *Biomed. Opt. Express* **6**(9), 3313–3319 (2015).
27. B. Vakoc, S. Yun, J. de Boer, G. Tearney, and B. Bouma, "Phase-resolved optical frequency domain imaging," *Opt. Express* **13**(14), 5483–5493 (2005).
28. A. B. Vakhtin, D. J. Kane, W. R. Wood, and K. A. Peterson, "Common-path interferometer for frequency-domain optical coherence tomography," *Appl. Opt.* **42**(34), 6953–6958 (2003).
29. H. Fizeau, *Recherches sur les modifications que subit la vitesse de la lumière dans le verre et plusieurs autres corps solides sous l'influence de la chaleur* (Mallet-Bachelier, Imprimeur-Libraire, 1862).
30. D. J. Gauthier, R. W. Boyd, R. K. Jungquist, J. B. Lisson, and L. L. Voci, "Phase-conjugate Fizeau interferometer," *Opt. Lett.* **14**(6), 323–325 (1989).
31. X. Liu, I. I. Iordachita II, X. He, R. H. Taylor, and J. U. Kang, "Miniature fiber-optic force sensor based on low-coherence Fabry-Pérot interferometry for vitreoretinal microsurgery," *Biomed. Opt. Express* **3**(5), 1062–1076 (2012).
32. U. Sharma and J. U. Kang, "Common-path optical coherence tomography with side-viewing bare fiber probe for endoscopic optical coherence tomography," *Rev. Sci. Instrum.* **78**(11), 113102 (2007).
33. X. Li, J.-H. Han, X. Liu, and J. U. Kang, "Signal-to-noise ratio analysis of all-fiber common-path optical coherence tomography," *Appl. Opt.* **47**(27), 4833–4840 (2008).
34. J.-U. Kang, J.-H. Han, X. Liu, and K. Zhang, "Common-path optical coherence tomography for biomedical imaging and sensing," *J. Opt. Soc. Korea* **14**(1), 1–13 (2010).
35. B. F. Kennedy, R. A. McLaughlin, K. M. Kennedy, L. Chin, A. Curatolo, A. Tien, B. Latham, C. M. Saunders, and D. D. Sampson, "Optical coherence micro-elastography: mechanical-contrast imaging of tissue microstructure," *Biomed. Opt. Express* **5**(7), 2113–2124 (2014).
36. Y. Qiu, Y. Wang, Y. Xu, N. Chandra, J. Haorah, B. Hubbi, B. J. Pfister, and X. Liu, "Quantitative optical coherence elastography based on fiber-optic probe for in situ measurement of tissue mechanical properties," *Biomed. Opt. Express* **7**(2), 688–700 (2016).
37. W. Shang, K. V. Larin, L. Jiasong, S. Vantipalli, R. K. Manapuram, S. Aglyamov, S. Emelianov, and M. D. Twa, "A focused air-pulse system for optical-coherence-tomography-based measurements of tissue elasticity," *Laser Phys. Lett.* **10**, 075605 (2013).

38. S. Wang and K. V. Larin, "Shear wave imaging optical coherence tomography (SWI-OCT) for ocular tissue biomechanics," *Opt. Lett.* **39**(1), 41–44 (2014).
39. C. Wu, Z. Han, S. Wang, J. Li, M. Singh, C. H. Liu, S. Aglyamov, S. Emelianov, F. Manns, and K. V. Larin, "Assessing age-related changes in the biomechanical properties of rabbit lens using a coaligned ultrasound and optical coherence elastography system," *Invest. Ophthalmol. Vis. Sci.* **56**(2), 1292–1300 (2015).
40. J. Li, S. Wang, M. Singh, S. Aglyamov, S. Emelianov, M. D. Twa, and K. V. Larin, "Air-pulse OCE for assessment of age-related changes in mouse cornea in vivo," *Laser Phys. Lett.* **11**, 065601 (2014).
41. J. Li, S. Wang, M. Singh, S. Aglyamov, S. Emelianov, M. Twa, and K. Larin, "Air-pulse OCE for assessment of age-related changes in mouse cornea in vivo," *Laser Phys. Lett.* **11**, 065601 (2014).
42. D. G. Altman and J. M. Bland, "Measurement in medicine: the analysis of method comparison studies," *Statistician* **32**, 307–317 (1983).
43. Z. Han, J. Li, M. Singh, C. Wu, C. H. Liu, S. Wang, R. Idugboe, R. Raghunathan, N. Sudheendran, S. R. Aglyamov, M. D. Twa, and K. V. Larin, "Quantitative methods for reconstructing tissue biomechanical properties in optical coherence elastography: a comparison study," *Phys. Med. Biol.* **60**(9), 3531–3547 (2015).
44. I. S. Sokolnikoff and R. D. Specht, *Mathematical Theory of Elasticity* (McGraw-Hill New York, 1956), Vol. 83.
45. J. F. Doyle, "Wave propagation in structure: spectral analysis using fast discrete Fourier transforms," Springer-Verlag, New York (1997).
46. M. Singh, C. Wu, C. H. Liu, J. Li, A. Schill, A. Nair, and K. V. Larin, "Phase-sensitive optical coherence elastography at 1.5 million A-Lines per second," *Opt. Lett.* **40**(11), 2588–2591 (2015).
47. V. Fathipour, T. Schmoll, A. Bonakdar, S. Wheaton, and H. Mohseni, "Demonstration of Shot-noise-limited Swept Source OCT Without Balanced Detection," *Sci. Rep.* **7**(1), 1183 (2017).
48. R. K. Manapuram, V. G. R. Manne, and K. V. Larin, "Phase-sensitive swept source optical coherence tomography for imaging and quantifying of microbubbles in clear and scattering media," *J. Appl. Phys.* **105**, 1–10 (2009).
49. R. K. Manapuram, V. G. R. Manne, and K. V. Larin, "Development of phase-stabilized swept-source OCT for the ultrasensitive quantification of microbubbles," *Laser Phys.* **18**, 1080–1086 (2008).
50. C. H. Liu, A. Schill, R. Raghunathan, C. Wu, M. Singh, Z. Han, A. Nair, and K. V. Larin, "Ultra-fast line-field low coherence holographic elastography using spatial phase shifting," *Biomed. Opt. Express* **8**(2), 993–1004 (2017).
51. W. Qi, R. Li, T. Ma, J. Li, K. Kirk Shung, Q. Zhou, and Z. Chen, "Resonant acoustic radiation force optical coherence elastography," *Appl. Phys. Lett.* **103**(10), 103704 (2013).
52. R. K. Manapuram, V. G. R. Manne, and K. V. Larin, "Development of phase-stabilized swept-source OCT for the ultrasensitive quantification of microbubbles," *Laser Phys.* **18**, 1080–1086 (2008).
53. R. K. Manapuram, V. G. R. Manne, and K. V. Larin, "Phase-sensitive swept source optical coherence tomography for imaging and quantifying of microbubbles in clear and scattering media," *J. Appl. Phys.* **105**, 102040 (2009).
54. Z. Han, M. Singh, S. R. Aglyamov, C. H. Liu, A. Nair, R. Raghunathan, C. Wu, J. Li, and K. V. Larin, "Quantifying tissue viscoelasticity using optical coherence elastography and the Rayleigh wave model," *J. Biomed. Opt.* **21**(9), 90504 (2016).
55. M. Singh, J. Li, S. Vantipalli, Z. Han, K. V. Larin, and M. D. Twa, "Optical coherence elastography for evaluating customized riboflavin/UV-A corneal collagen crosslinking," *J. Biomed. Opt.* **22**(9), 91504 (2017).
56. A. B. Vakhtin, D. J. Kane, W. R. Wood, and K. A. Peterson, "Common-path interferometer for frequency-domain optical coherence tomography," *Appl. Opt.* **42**(34), 6953–6958 (2003).
57. K. Zhang, W. Wang, J. Han, and J. U. Kang, "A surface topology and motion compensation system for microsurgery guidance and intervention based on common-path optical coherence tomography," *IEEE Trans. Biomed. Eng.* **56**(9), 2318–2321 (2009).
58. J. U. Kang, J. H. Han, X. Liu, and K. Zhang, "Common-Path Optical Coherence Tomography for Biomedical Imaging and Sensing," *J. Opt. Soc. Korea* **14**(1), 1–13 (2010).
59. U. Sharma and J. U. Kang, "Common-path optical coherence tomography with side-viewing bare fiber probe for endoscopic optical coherence tomography," *Rev. Sci. Instrum.* **78**(11), 113102 (2007).
60. C. Li, G. Guan, Z. Huang, M. Johnstone, and R. K. Wang, "Noncontact all-optical measurement of corneal elasticity," *Opt. Lett.* **37**(10), 1625–1627 (2012).
61. Ł. Ambroziński, S. Song, S. J. Yoon, I. Pelivanov, D. Li, L. Gao, T. T. Shen, R. K. Wang, and M. O'Donnell, "Acoustic micro-tapping for non-contact 4D imaging of tissue elasticity," *Sci. Rep.* **6**, 38967 (2016).
62. C. Li, G. Guan, R. Reif, Z. Huang, and R. K. Wang, "Determining elastic properties of skin by measuring surface waves from an impulse mechanical stimulus using phase-sensitive optical coherence tomography," *J. R. Soc. Interface* **9**(70), 831–841 (2012).
63. T. M. Nguyen, A. Zorgani, M. Lescanne, C. Boccara, M. Fink, and S. Catheline, "Diffuse shear wave imaging: toward passive elastography using low-frame rate spectral-domain optical coherence tomography," *J. Biomed. Opt.* **21**(12), 126013 (2016).
64. B. Park, M. C. Pierce, B. Cense, S. H. Yun, M. Mujat, G. Tearney, B. Bouma, and J. de Boer, "Real-time fiber-based multi-functional spectral-domain optical coherence tomography at 1.3  $\mu\text{m}$ ," *Opt. Express* **13**(11), 3931–3944 (2005).

65. J. A. Izatt, M. A. Choma, and A.-H. Dhalla, "Theory of optical coherence tomography," in *Optical Coherence Tomography: Technology and Applications*, W. Drexler and J. G. Fujimoto, eds. (Springer International Publishing, Berlin, 2015), pp. 65–94.
66. L. An, P. Li, G. Lan, D. Malchow, and R. K. Wang, "High-resolution 1050 nm spectral domain retinal optical coherence tomography at 120 kHz A-scan rate with 6.1 mm imaging depth," *Biomed. Opt. Express* **4**(2), 245–259 (2013).
67. P. Li, L. An, G. Lan, M. Johnstone, D. Malchow, and R. K. Wang, "Extended imaging depth to 12 mm for 1050-nm spectral domain optical coherence tomography for imaging the whole anterior segment of the human eye at 120-kHz A-scan rate," *J. Biomed. Opt.* **18**(1), 016012 (2013).
68. G. Lan and G. Li, "Design of a k-space spectrometer for ultra-broad waveband spectral domain optical coherence tomography," *Sci. Rep.* **7**, 42353 (2017).
69. W. Drexler, M. Liu, A. Kumar, T. Kamali, A. Unterhuber, and R. A. Leitgeb, "Optical coherence tomography today: speed, contrast, and multimodality," *J. Biomed. Opt.* **19**(7), 071412 (2014).

## 1. Introduction

A hallmark of disease is a change in the physical properties of affected tissues, e.g. change in stiffness due to tumor, swelling, or inflammation [1, 2]. Elastography imaging, sometimes referred to as *digital palpation*, was originally developed as a non-invasive assessment method to detect subtle changes in tissue stiffness caused by tumors in soft tissue [3, 4]. Optical coherence elastography (OCE) is one of several elasticity imaging techniques designed to provide quantitative measurements of tissue biomechanical properties [5]. Because it is based on optical interferometry, OCE offers greater axial and lateral spatial resolution, compared to ultrasound elastography [6–8], or magnetic resonance elastography [9, 10]. The promise of this non-invasive imaging-based technology is that it can provide quantitative, *in vivo* diagnostic information that may be useful for earlier disease detection and more precise guidance on the response to treatment [4].

Optical coherence elastography is comprised of a static or dynamic sample loading system to induce tissue displacement and a high-resolution optical coherence tomography (OCT) imaging system to detect the resulting tissue deformation. OCT imaging is a form of low-coherence interferometry where the interference signal is generated by combining light from reference and sample arms to provide micron-level spatial resolution in both lateral and axial dimensions [11]. In the original work of static OCE [5], structural OCT imaging was used for the deformation assessment. However, if the tissue deformation induced during elastography imaging is on the order of microns or less, it may fall below the detection capabilities of structural OCT imaging. By analyzing the complex component of the OCT signal, phase-sensitive OCT (PhS-OCT) [12–16] can provide much greater sample displacement sensitivity (nanometer-scale) [3, 12, 17–22] and direct quantitative measurements of the displacement along the optical axis, which enables the visualization and analysis of the shear wave propagation in dynamic OCE [4, 23].

Poor phase stability (micron-scale amplitude) can limit the system performance of dynamic elastography imaging and there are a number of potential sources of environmental, electromechanical, and optical noise that can reduce optical phase stability. Vibrational instability (e.g. induced by seismic vibration, acoustic vibration, direct-force vibration etc.) [24] can exist between the sample and reference arms and is a major source of optical phase fluctuations. Vibration causes relative axial motion between two optical paths and can alter the interference path difference during image acquisition [25]. Post-acquisition, digital signal processing methods (e.g. Fourier analysis, wavelet de-noising, and band-pass filtering) are effective to subtract background noise and improve the signal-to-noise ratio (SNR). This approach relies on distinctive features (e.g. frequencies and amplitudes) that help make the signal and noise separable. Optical solutions to enhance phase stability at the source of the signal are preferred (e.g. calibration by a second phase signal [26, 27]) and can be combined with post acquisition signal processing.

Common-path OCT [28] (similar to Fizeau interferometry [29, 30]) is one optical method to provide stable phase signal in a simpler and more compact configuration where the sample and reference arms share a common optical path with a reference plane defined by an optical

surface proximal to the sample. Common-path OCT provides intrinsic compensation for polarization mismatch and dispersion mismatch induced by optical elements (e.g. fiber and lens) [28]. Common-path OCT can effectively reduce the imaging system's susceptibility to vibration, thereby increasing the system's physical stability and optical phase sensitivity [31]. A common-path design can integrate the reference plane into a sample probe of single mode fiber with arbitrary length, which allows highly miniaturized probes for endoscopic OCT, intravascular OCT, or surgical tools [31–34]. While common-path OCT has been described for structural OCT imaging, and static phase-sensitive OCE [35, 36], its value for dynamic phase-sensitive elastography imaging has not been evaluated.

The contribution of this research is to describe the development and use of a common-path PhS-OCT system for dynamic elastography imaging that can distinguish micron-scale (or sub-micron-scale) elastic waves induced in tissue. This design provides a more stable reference platform for optical phase measurements, enhanced surface displacement measurement precision, as well as a simpler and more compact system configuration that can help advance laboratory and clinical elastography studies.

## 2. Common-path phase sensitive optical coherence elastography

We recently constructed a common-path PhS-OCE system ( $OCE_{CP}$ ) by making modifications to our custom-built spectral-domain PhS-OCE (referred to as conventional PhS-OCE, or  $OCE_{COV}$  here), as shown in Fig. 1. This PhS-OCE was situated on an optical table that was not floated or actively damped. Modifications included elimination of the conventional reference arm (using a simple shutter here) and insertion of a reference plate between the scan lens and sample. The reference plane is the sample-side optical surface of the reference plate, where M-mode imaging (repeated A-scan acquisitions over time at the same location) was possible by both methods:  $OCE_{COV}$  and  $OCE_{CP}$ . The switch between conventional and common-path OCE configurations was done within seconds.

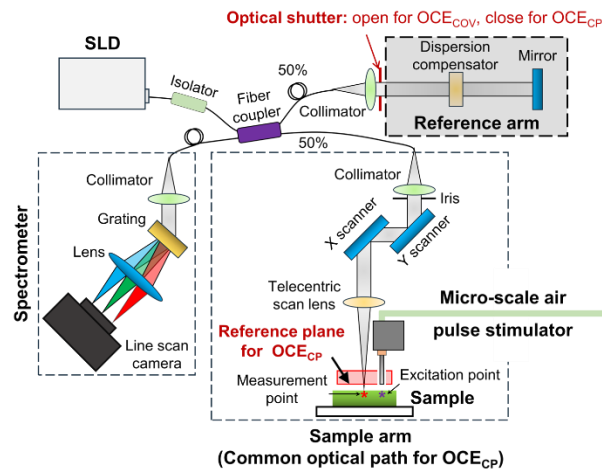


Fig. 1. Schematic of the custom-built phase-sensitive optical coherence elastography (PhS-OCE) system, comprised of a micro-scale air pulse stimulator to induce tissue mechanical waves and a high-resolution spectral domain optical coherence tomography (SD-OCT) imaging system to detect the resulting tissue deformation. Common-path OCT was constructed based on conventional OCT by blocking the reference arm and inserting a optically flat reference plate between the telecentric scan lens and sample. The reference plane was the sample-side optical surface of the reference plate.

The light source used in both OCT systems was a superluminescent laser diode (SLD, D-855, Superlum Diodes Ltd.) with a waveband of 795 nm – 895 nm, centered at 845 nm. In the conventional OCT configuration, the SLD output was split by a fiber coupler at a ratio of



50:50 into the sample and reference arms. In the sample arm, the input light diameter was up to 4 mm, controlled by an iris; the focal length of the telecentric scan lens was 54 mm, and the working distance was 42.3 mm. When the iris was fully open, the maximum light power at the sample arm focal plane was ~4.6 mW. In the reference arm, a dispersion compensator was used to match the dispersion of the scan lens. The returned beams from both arms were collected by a spectrometer, consisting of a collimator with 100 mm focal length, a grating with 1800 lines/mm, a focusing lens group with 130 mm focal length, and a line scan camera (spL4096-140kmESC, Basler) with  $4096 \times 2$  pixels. The axial resolution was ~3.3  $\mu\text{m}$ , the lateral resolution was ~7.8  $\mu\text{m}$ , and the maximum imaging depth was ~6.76 mm (all calculated in air).

In the common-path OCT configuration, the reference plane was the optical surface of the reference plate proximal to the sample. The reference plate and sample shared a common light path, providing the same polarization and dispersion properties and reducing the phase instability caused by the relative motion between the reference and sample (0.3 mm – 6.76 mm axial distance in air). The scan lens was in a telecentric configuration so that the chief rays of different scan locations were parallel to the optical axis and perpendicular to the reference plate. A 5-mm thick, optically flat acrylic plate was used as the reference plate in the common-path OCT configuration. The optical path length of the plate (~7.42 mm) was longer than the OCT depth range (~6.76 mm) so that the optical surface distal to the sample did not contribute to the spectral interferogram. The light power exposed to the reference plane and sample was simultaneously controlled by an iris, and the maximum light power measured after the reference plate was ~4.2 mW. The maximum measured signal sensitivity was 102.4 dB and the maximum axial sensitivity fall-off was -36.0 dB at 6.66 mm. The -6 dB fall-off position was ~3 mm.

A micro-scale air-pulse stimulator was applied to provide a short duration ( $\leq 1$  ms) [37], localized tissue excitation that was normal to the sample surface. Medical grade air was supplied to a solenoid valve and delivered to the sample through a cannula (inner diameter: 150  $\mu\text{m}$ ). The air pulse pressure (sample stimulation) was controlled over a range, from 0 Pa – 100 Pa. The air delivery system was designed to minimize interference with the optical path and this allowed both conventional and common-path OCE. The air-pulse was synchronized with the OCT imaging system [38] and the air cannula was precisely positioned using a three-dimensional (3-D) micrometer stage.

### 3. Phase stability evaluation

#### 3.1 Measurement methods

In OCE measurements, phase changes can be detected as sub-pixel motion along the optical axis. These observed phase differences include background phase noise (system instability) as well as induced sample displacements during elastography measurements. Phase information at a specified axial depth  $\varphi_z(t_J - t_0)$  can be resolved and unwrapped by tracing one point from time  $t_J$  to the referenced time point  $t_0$  among the successive A-scan signals. The change in axial displacement for the sample surface in air,  $\Delta z(t_J - t_0)$ , is therefore represented by the observed phase change using Eq. (1), where  $\lambda_0$  is the center wavelength [20].

$$\Delta z(t_J - t_0) = \frac{\lambda_0}{4\pi} \times \varphi_z(t_J - t_0) \quad (1)$$

Since measurements were only made from the sample surface, there was no need for physical rescaling by refractive index nor surface motion and refractive index mismatch error correction [20]. A mirror served as the sample to evaluate phase stability for both conventional OCE (OCE<sub>COV</sub>) and common-path OCE (OCE<sub>CP</sub>) methods. Phase noise was quantified for each method under the same measurement conditions ( $n = 9$ ). The temporal resolution was 15  $\mu\text{s}$  and the total measurement period was 90 ms for each test.

### 3.2 Measurement results

The phase noise was measured, quantified, and compared for both conventional OCE ( $OCE_{COV}$ ) and common-path OCE ( $OCE_{CP}$ ) methods in Fig. 2. The noise amplitude was reduced by several orders of magnitude (from micrometer to sub-nanometer level) for the low-frequency ( $\sim 21$  Hz) phase component in  $OCE_{CP}$  measurement compared to  $OCE_{COV}$  measurement.

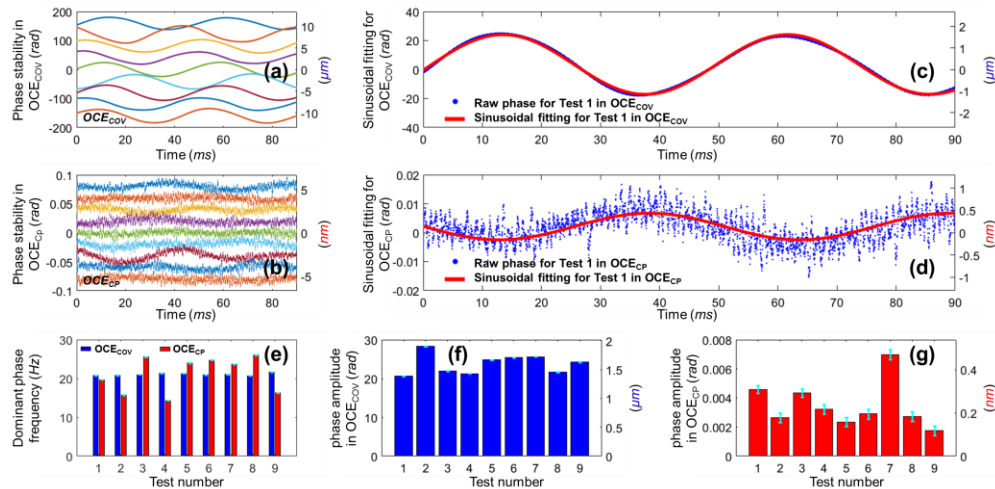


Fig. 2. Common-path OCE ( $OCE_{CP}$ ) has greater phase stability than conventional OCE ( $OCE_{COV}$ ). Phase noise was quantified with a mirror for both OCE methods ( $n = 9$  measures). Panel (a)  $OCE_{COV}$  and (b)  $OCE_{CP}$  are the measured phase fluctuations, plotted from top to bottom with offset values between repeated measurements for better visualization. Panel (c) and (d) demonstrate the low-frequency sinusoidal pattern of background noise as the dominant component for both  $OCE_{COV}$  and  $OCE_{CP}$  (note the different y-axes). Panel (e) compares the noise frequency ( $\sim 21$  Hz), which is similar for both OCE methods. Panels (f) and (g) show, a reduction of phase noise amplitude by method: (f) micrometer level in  $OCE_{COV}$ ; (g) sub-nanometer level in  $OCE_{CP}$ .

Measured phase fluctuations are shown in Fig. 2(a) for  $OCE_{COV}$  and in Fig. 2(b) for  $OCE_{CP}$ . Each measurement ( $n = 9$ ) was shifted along the vertical axis to reduce overlap and improve visualization. The dominant component of the phase variation measurement was a low-frequency periodic signal that had been previously identified as environmental turbulence (predominantly vibrations) between the sample and reference arms. Similar low-frequency phase variations were observed in both OCE methods, but the amplitude was reduced significantly in  $OCE_{COV}$  ( $\sim 0.3$  nm), versus  $OCE_{CP}$  measurements ( $\sim 1.6$   $\mu$ m).

A first-order sinusoidal curve was fitted to describe the dominant frequency and amplitude components of the observed phase fluctuations (Curve fitting toolbox, Matlab R2016a, MathWorks, Inc. Natick, Massachusetts). Two examples are shown in Figs. 2(c) and 2(d), for the first phase measurements for each OCE method. The phase noise was fitted to sinusoidal curves with mean 95% confidence interval (CI) fitting errors of  $\pm 0.0083$  Hz and  $\pm 0.4233$  Hz in frequency, and 0.0322 radians (2.2 nm displacement) and 0.32 milliradians (0.02 nm displacement) in amplitude for the  $OCE_{COV}$  and  $OCE_{CP}$  measurements respectively.

Figure 2(e) compares the fitted dominant frequencies for the phase noise acquired from each OCE method. The measured noise frequency in  $OCE_{COV}$  was 20.68 – 21.62 Hz (95% CI:  $21.05 \pm 0.20$  Hz). The measured noise frequency in  $OCE_{CP}$  was 14.32 – 26.02 Hz (95% CI:  $21.01 \pm 3.03$  Hz). Both OCE measurement methods showed a  $\sim 21$  Hz vibrational turbulence, which is likely to be environmental noise. Figures 2(f) and 2(g) compare the fitted amplitudes of the phase noise acquired from both OCE methods. The measured noise amplitude in  $OCE_{COV}$  was 20.60 – 28.36 radians (95% CI:  $23.77 \pm 1.67$  radians), which corresponds to

1.39 – 1.91  $\mu\text{m}$  (95% CI:  $1.60 \pm 0.11 \mu\text{m}$ ). The measured noise amplitude in  $\text{OCE}_{\text{CP}}$  was 1.8 – 7.0 milliradians (95% CI:  $3.5 \pm 1.05$  milliradians), which corresponds to 0.12 – 0.47 nm (95% CI:  $0.24 \pm 0.07 \text{ nm}$ ). The common-path technique reduced the amplitude of the dominant low-frequency noise component from tens of radians (micrometer scale) in conventional PhS-OCE to milliradians (sub-nanometer scale) in common-path PhS-OCE.

In addition to assessing phase stability at one axial position, we evaluated phase-stability over a depth range (0.33 mm to 6.66 mm). The data show that phase stability (mean  $\pm$  SD) changed little over the full range ( $3.54 \pm 0.61$  milliradians, corresponding to  $0.24 \pm 0.04 \text{ nm}$ ,  $n = 400$ ; 20 repeated measurements at 20 different axial positions).

## 4. Elastography measurement methods

### 4.1 Surface displacement dynamics

During OCE measurements, the air-pulse stimulus generated a localized low-amplitude (micron or sub-micron) displacement that then induced mechanical waves within the sample [37], as seen in Fig. 3. With M-mode imaging, the observed temporal surface displacement dynamics include: (1) a baseline period before sample excitation, (2) an initial negative surface displacement signal (primary deformation) that is driven by the air-pulse excitation force, (3) a recovery response period where the sample surface returns to its original position, and (4) a period of damped oscillatory motion [39, 40].

In this study, we measured the primary surface displacement response to an applied force for conventional and common-path OCE. We have previously shown that this response is related to the sample's mechanical properties (e.g. stiffer samples deform less under the same load) [18].

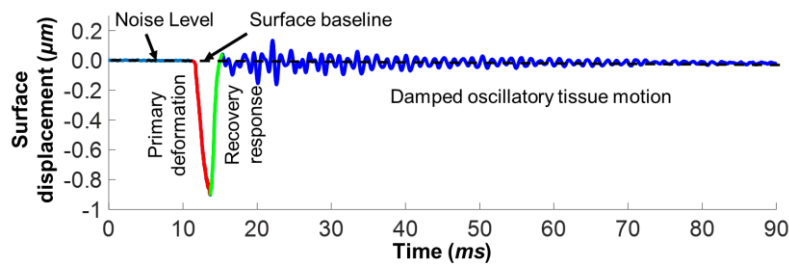


Fig. 3. Typical M-mode surface displacement dynamics include: a baseline period before sample excitation that represents the noise level, an initial negative primary surface displacement (red) that is driven by the excitation force, a recovery response (green) that relates to sample viscoelasticity, and a period of damped oscillatory motion (blue). This example was acquired from a 2% agar phantom by common-path OCE (applied pressure: 12 Pa).

### 4.2 Measurement methods

M-mode detection was performed to evaluate the precision of the primary axial displacement amplitude (spatial resolution:  $0.24 \pm 0.07 \text{ nm}$ , temporal resolution: 15  $\mu\text{s}$ ). The tip of the micro air-pulse stimulator (150  $\mu\text{m}$  in diameter) was kept  $\sim 0.5 \text{ mm}$  from the surface of the sample to reduce any near-field influence [41]. The stimulation pressure was increased from 4 Pa to 32 Pa with a step of 4 Pa to generate mechanical responses ranging from small to large primary displacements in the 2% agar phantom. Focused air-pulses for each air pressure were repeated 5 times over a 2.0 s period. Phantom surface responses were detected in the center of the phantom and at a lateral distance of  $\sim 0.3 \text{ mm}$  from the excitation point. The air-pulse stimulus was triggered at 10 ms over a total OCE measurement period of 90 ms. Surface displacement was converted from phase based on Eq. (1). The duration of the primary displacement and recovery process were approximately 4 ms and depended upon the stimulus pressure.



In conventional OCE measurements, the primary displacements were quantified with and without digital filtering. For the unfiltered data from conventional OCE ( $OCE_{COV}$ ) measurements, we calculated the primary surface displacement amplitude as the magnitude of the maximum primary deformation response relative to the absolute phase when the deformation started to occur. For the digital-filtered samples ( $OCE_{COV + FLT}$ ), primary displacement amplitude was calculated in the same way after digital filtering. A fast-Fourier transform was used to fit and subtract the dominant frequency component of the background noise (Matlab R2016a, MathWorks, Inc. Natick, Massachusetts). In common-path OCE ( $OCE_{CP}$ ) measurement, the primary surface displacement was calculated directly as there was negligible (less than 1 nm) low-frequency background noise by this measurement method.

Measurement precision was compared based on the absolute measurement values and the coefficient of variation (CV: standard deviation divided by the mean) for the measured primary deformation amplitude from  $OCE_{COV}$ ,  $OCE_{COV + FLT}$ , and  $OCE_{CP}$ . We defined a criterion of  $CV \leq 5\%$  as acceptable measurement precision. We also plotted the 95% limits of agreement [42] to compare each OCE measurement method ( $OCE_{COV}$ ,  $OCE_{COV + FLT}$ , and  $OCE_{CP}$ ) and to describe the residual difference between each method.

### 4.3 Agar tissue phantoms

Displacement comparisons for OCE measurement methods were performed with 2% agar samples, prepared in 35 mm petri dishes [19, 43]. These tissue-mimicking phantoms were prepared, sealed, and cooled in a refrigerator overnight before use. We controlled the weight of the solution to ensure consistency when preparing the phantoms (errors  $\leq \pm 0.01\%$ ). We also tracked the temperature and weight of the phantoms during the experiment to account for any evaporation, dehydration (0.01% – 0.04%), or environmental effects.

### 4.4 Measurement results

Surface displacements are plotted in Figs. 4(a)-4(c) with air-pulse pressures ranging from 4 Pa (top) to 32 Pa (bottom); each displacement profile was shifted to reduce overlap. Our total measurement period included a pre-stimulation period (12 ms), a stimulation and recovery period (from 12 to 15 ms), and a post-stimulation period ( $> 15$  ms). This long measurement period was designed to capture the temporal surface displacement dynamics before, during, and after sample stimulation. Figure 4(a) shows the raw  $OCE_{COV}$  surface displacement data. The background noise (mean  $\pm$  95% CI:  $20.61 \pm 0.52$  Hz.) can clearly be observed and was filtered as described earlier. The new surface displacement dynamic after digital filtering ( $OCE_{COV + FLT}$ ) is plotted in Fig. 4(b). The majority of the background phase noise was removed, but there was still some low-amplitude residual disturbances (sub-micron) that could affect measurement precision. Figure 4(c) shows the raw  $OCE_{CP}$  surface displacement data. The phase stability was improved to a sub-nanometer level in  $OCE_{CP}$  and is hard to observe relative to the primary displacement amplitude on this plotting scale.

Figure 4(d) shows the primary deformation amplitude from each method. The amplitude of the primary displacement increased ( $\sim 0.20 - 4.03 \mu\text{m}$ ) upon increasing air-pulse pressure (4–32 Pa). For each test under any air-pulse stimulus pressure, the distribution of the primary displacements was the smallest with  $OCE_{CP}$ .

Figure 4(e) shows the coefficient of variation (CV) for the measured primary deformation in each test. Using the raw data from  $OCE_{COV}$ , all calculated CVs for the measured primary deformation responses were greater than the 5% threshold. For the data from  $OCE_{COV + FLT}$  with moderate sample stimulation pressure (12 – 24 Pa), moderate sample deformations ( $\sim 0.87 - 2.82 \mu\text{m}$ ) were produced and the average CV was 3.5%. However, the CV was comparatively large (18.6%) for small surface deformations ( $\sim 0.2 - 0.54 \mu\text{m}$ ) produced by small sample stimulation pressures (4 – 8 Pa). Similarly, large deformation amplitudes ( $\sim 3.36 - 4.03 \mu\text{m}$ ) were produced by larger sample stimulation pressures (28 – 32 Pa) and these were

more variable (CV = 11.0%). Surface primary displacements measured using  $OCE_{CP}$  were consistently small; all CVs were less than 5% with an average value of 1.89%.

In Figs. 4(d) and 4(e), common-path OCE provides a larger dynamic detection range with higher detection sensitivity in surface displacement measurement than conventional PhS-OCE.

Figure 4(f) shows good agreements among these three measurement methods. The pair of  $OCE_{COV}$  and  $OCE_{CP}$  and the pair of  $OCE_{COV+FLT}$  and  $OCE_{CP}$  have similar biases and similar limits of agreements that ( $\text{mean} \pm 1.96\text{SD}$ ) were  $0.049 \pm 0.272 \mu\text{m}$  and  $0.018 \pm 0.248 \mu\text{m}$  respectively.

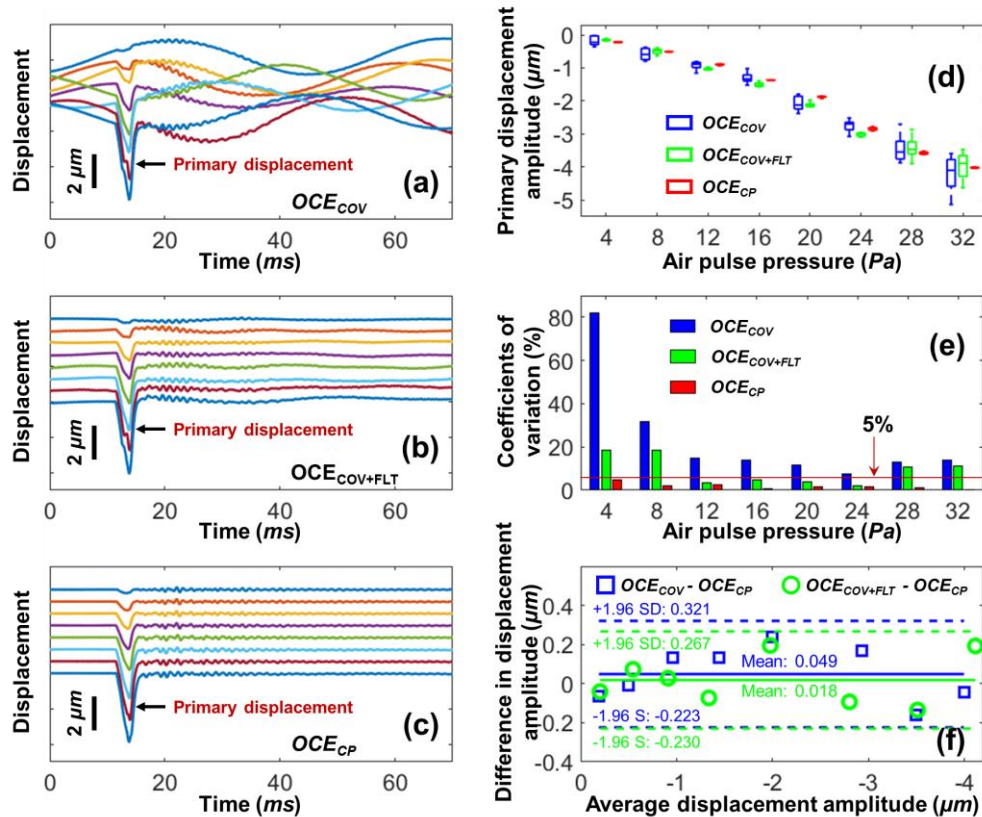


Fig. 4. Common-path OCE has greater surface displacement detection sensitivity than conventional OCE. Surface displacements were measured in a 2% agar phantom and compared for both OCE methods (M-mode,  $n = 5$  repeated measures, at 8 different excitation pressures [4 to 32 Pa: color series]). Displacements were measured 0.3 mm from the excitation point. Panel (a) shows raw surface displacement measurements by conventional OCE ( $OCE_{COV}$ ). Sinusoidal low-frequency background noise was clearly observed. (b) Digital filtering methods ( $OCE_{COV+FLT}$ ) can reduce this noise. (c) Raw displacement by common-path OCE ( $OCE_{CP}$ ) shows greater phase stability (sub-nanometer level). (d) Primary displacement amplitude variability increases with excitation pressure amplitude ( $OCE_{COV} > OCE_{COV+FLT} > OCE_{CP}$ ). (e) Coefficients of variation (CV) for primary displacement amplitude were lowest for  $OCE_{CP}$  (mean: 1.89%). (f) Comparison of residual error (mean vs difference) shows good agreement among measurement methods indicating no distinct bias between methods and similar 95% limits of agreement.

## 5. Mechanical property characterization with common-path OCE

Elastography measurements of material stiffness for 1%, 1.5%, and 2% agar tissue phantoms were performed using common-path OCE. The tissue phantoms were prepared in accordance with the procedure described in Section 4.3.

### 5.1 Methods

Agar phantoms deform when a load is applied, and return to their original location after the load is removed. Under the same load, stiffer samples tend to deform less. We measured the primary surface deformations 0.5 mm away from the stimulation point under the applied pressures (4 – 36 Pa; in a 4 Pa increment). The measurement was discontinued when the primary surface displacement reached ~6  $\mu\text{m}$  or when the maximal stimulation pressure was applied (36 Pa).

Young's modulus,  $E$ , is defined as the relationship between the stress and strain [44] and is a measure of elasticity. A larger value of Young's modulus is associated with greater sample stiffness (i.e. the sample deforms less under loading). Material stiffness can also be characterized based on the speed of elastic wave propagation within the sample. Our previous studies [18, 19, 43] have shown a good approximation for Young's modulus estimation in an isotropic homogeneous elastic material using the elastic wave group velocity,  $c$ , and the surface wave equation [45]:

$$E = \frac{2\rho(1+\nu)^3}{(0.87+1.12\nu)^2} c^2 \quad (2)$$

where  $\rho$  is the density,  $\nu$  is the Poisson's ratio, and  $c$  is the elastic wave group velocity. The agar phantoms' density ( $\rho$ ) and Poisson's ratio ( $\nu$ ) can be assumed as 1000  $\text{kg/m}^3$  and 0.5 [43]. The group velocity of the elastic surface wave was quantified by  $c = d/t$ , where  $d$  and  $t$  are the distance and the time delay of the primary surface displacement between two measurement points, respectively

We measured elastic wave propagation speeds in 1%, 1.5%, and 2% agar phantoms to determine the mechanical properties of each sample (stimulation pressure: 16 Pa). The sample deformation responses were measured at 1 mm increments, 0.3 mm to 5.3 mm away from the stimulation point. The elastic wave propagation speed was calculated by the time delay at each measurement location from the excitation position ( $n = 5$  repeated measurements at each location).

### 5.2 Results

Figure 5(a) shows the resulting primary deformation responses for the 1%, 1.5%, and 2% agar phantoms. The primary deformation decreased with the increasing agar concentration at the same pressure. The slope between the primary deformations and the applied pressures can be used to distinguish samples with different stiffness. The fitted slopes (mean  $\pm$  95% CI) were:  $0.32 \pm 0.07 \mu\text{m/Pa}$  (1%),  $-0.19 \pm 0.02 \mu\text{m/Pa}$  (1.5%), and  $-0.08 \pm 0.01 \mu\text{m/Pa}$  (2%).

Figure 5(b) shows the calculated group velocities, which were (mean  $\pm$  95% CI)  $2.75 \pm 0.12 \text{ m/s}$  (1%),  $3.88 \pm 0.19 \text{ m/s}$  (1.5%), and  $5.93 \pm 0.23 \text{ m/s}$  (2%) respectively for agar phantoms. The group velocity of the wave increased with increasing concentration of agar.

Figure 5(c) shows the estimated Young's moduli for the 1%, 1.5%, and 2% agar phantoms based on group velocities (Eq. (2), which were (mean  $\pm$  95% CI)  $24.96 \pm 2.18 \text{ kPa}$  (1%),  $49.69 \pm 4.87 \text{ kPa}$  (1.5%), and  $116.08 \pm 12.14 \text{ kPa}$  (2%) respectively for agar phantoms. The group velocities of the surface waves and the estimated Young's moduli for the agar phantoms were consistent with our previous published results [43].

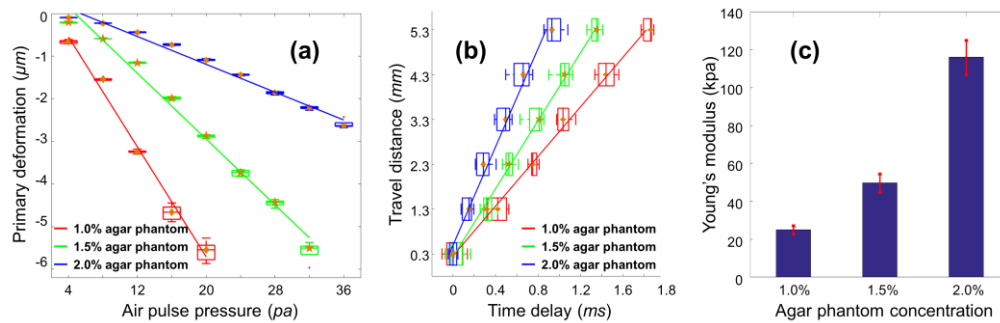


Fig. 5. Stiffness characterization by common-path OCE ( $\text{OCE}_{\text{CP}}$ ) in 1%, 1.5%, and 2% agar phantoms ( $n = 5$  repeated measures per sample). (a) The primary deformation decreases with increasing agar concentration under the same air-pulse pressure. The measurement point was 0.5 mm away from the stimulation point. (b) The surface wave had faster group velocities with higher agar concentration. (c) Estimation of Young's modulus, based on wave propagation velocities in (b) and Eq. (2), shows stiffness increases with agar concentration.

## 6. Discussion

We used a spectral domain OCT system in this study due to the inherently stable phase signal of the SLD light source. Recently, swept-source light sources with multi-MHz A-scan rates have been developed [22, 46], which enables nearly real-time optical elastography, which will enable detection of elastic wave propagation with single-shot excitation. This common-path strategy can be easily implemented for swept-source OCT/OCE imaging modalities to reduce the effect of the local vibration existing between the sample and reference arms, and thus to enhance the system's phase stability. A common-path strategy can be implemented for swept-source OCT/OCE imaging modalities using a single photodetector, such as demonstrated by Fathipour and colleagues [47]. In addition to standard methods of phase-noise cancellation in SS-OCT systems, such as optical setups with synchronized optical and data acquisition triggering [48, 49], a common-path configuration can further enhance the system's phase stability [22]. Another single-shot optical elastography technique has been demonstrated by utilizing a line focused probe beam [50], which could also benefit from common path optics to increase system stability and sensitivity.

The measured phase stability in our common-path design is 3.5 milliradians (corresponding to 0.24 nm of displacement). This level of phase stability was achieved without any stabilization systems (e.g. floated optical table, active damping, etc.). The residual phase variation is mainly determined by the electrical hardware (e.g. SLD light source). Previous publications using conventional SD-OCT have shown similar phase stability performance [14, 15, 51]. Stabilization and vibration-isolation devices are commonly used to reduce vibrational noise from the separate sample and reference arms in these conventional SD-OCT constructions. In most cases, phase stability measurements for OCT systems are determined using methods that are similar to our common-path optical design, i.e. stability measurements are derived from interference signals from two adjacent optical surfaces such as an optical plate [52, 53]. However, this same degree of phase-stability measured during ideal measurement conditions is not normally reported (or achieved) for conventional phase-resolved OCT imaging when separate sample and reference optical paths are used. Our results show that it is possible to achieve sub-nanometer phase-stability during dynamic elastography imaging of the sample by using a common-path optical design without any additional vibration-isolation devices or other compensation.

### 6.1 Advantages of common-path optical design

In this work, we have demonstrated that the use of a common-path optical design can greatly reduce the system noise and enhance displacement stability to a sub-nanometer scale ( $0.24 \pm$



0.07 nm). This enhanced stability thereby improves the system sensitivity for sample deformation detection and this will translate to better estimates of sample mechanical properties from elastography imaging.

This common-path OCE design has better precision (CV: 1.89%) for measurements of primary surface deformations over a large stimulus force range (4 – 32 Pa). We have successfully estimated Young's modulus for agar tissue phantoms of varying concentration based on elastic wave propagation speed. We have also used the correlation between the magnitude of primary displacement and the elastography stimulus force to distinguish agar phantoms of different stiffness. Greater measurement precision offered by this common-path optical design will improve estimates of material properties regardless of the mathematical model used to link the observed sample response to Young's modulus. Moreover, the enhanced system stability could allow for decreased stimulation forces, which is critical for ensuring safe *in vivo* elastographic measurements.

In addition to the primary deformation response, the stimulated agar samples exhibited a viscoelastic recovery response (Fig. 3) similar to what was reported in our previous publications [43, 54]. This recovery period is best characterized by an exponential decay function, from which we have previously described how to derive the sample's natural frequency based upon a kinematic model [39, 55]. From Figs. 4(a)–4(c), the common-path design is clearly a more stable platform from which to observe the entire dynamic response after stimulation. This approach can therefore provide a better basis to quantify sample viscoelasticity.

In common-path elastography imaging, we observed additional small amplitude (nanometer-scale) sample oscillations after the initial deformation response, which persisted for longer periods. These oscillations were damped and gradually decreased to zero (Fig. 3). It is possible to quantify these small-scale sample responses because of the improved phase-stability of the common-path design. These nanometer-scale displacements were difficult to visualize using conventional OCE. In comparison, these oscillations persist to the end of the observation time window (>70 ms) using OCE<sub>CP</sub> [Fig. 4(c)], but were undetectable after ~35 ms in OCE<sub>COV</sub> [Fig. 4(a)] and OCE<sub>COV + FLT</sub> [Fig. 4(b)]. At this point, the importance of these observations is not clear and their correlation with other tissue biomechanical properties such as damping behavior and natural frequency is the subject of future studies.

## 6.2 Disadvantages of common-path OCT

In phase-based displacement detection, common-path PhS-OCT has demonstrated superior capabilities over conventional PhS-OCT in phase stability, detection sensitivity, measurement precision and detection dynamic range.

In intensity-based (structure-based) detection, however, conventional OCT is advantageous over common-path OCT. In conventional OCT, the light power of both arms (sample and reference) can be adjusted independently, by means of using filters or irises, so that the reference arm can be used to modulate and optimize the interference signal for structural imaging. In common-path OCT, utilizing reference plates with different coatings on both sides (i.e. anti-reflection coating on the top surfaces, partially reflection coating on bottom surfaces with appropriate degrees of reflectivity) might be useful to optimize the signal [56]. Adjusting the reflective intensity from reference plane for interference signal optimization is still not as flexible and effective as adjusting the intensity from reference arm in conventional OCT [56–59]. Moreover, as the beam is scanned in common path OCT, the optical path lengths and point spread functions of different scan fields would create differences in the detection signal sensitivity, which would also limit the scanning range for structural imaging in common-path OCT.

Sample stimulation is usually required for OCE, which creates the possibility that the source of stimulation can interfere with optical sensing of the sample response. In common-path OCE, there is a tighter working space for installing the stimulation system since the



reference plate (plane) is inserted between the OCT objective lens and the sample (Fig. 1). Thus the common-path configuration posts more challenge on the physical compatibility between the set-ups of optical sensing and stimulation. This may not be problematic for optical [60] or ultrasound stimulation (e.g. acoustic micro-tapping technique [61]) due to the relative long stimulation delivery path, but may be an important system design consideration for contact mechanical loading [62] and other forms of non-contact physical stimulation with shorter delivery paths, e.g. air-pulse [37]. In some cases of static compression strain imaging, direct contact between the reference plane and the static loading can be performed [35, 36]. In most cases of dynamic OCE imaging, mechanical isolation between the optical path and the stimulation force is a crucial requirement for system construction. Passive elastography, on the other hand, can perform elastographic imaging using intrinsic motion in live samples and could also benefit from enhanced detection sensitivity of common path OCE [63].

### 6.3 Improving phase stability for faster volumetric OCE imaging

One fundamental limitation of phase stability and phase detection capability arises from the signal-to-noise ratio (SNR) of the intensity, reported as  $1/\sqrt{\text{SNR}}$  [64]. In SD-OCT, the depth-dependent loss in signal sensitivity (i.e. sensitivity “fall-off” [65]) leads to weaker sensitivity in deeper imaging regions [66–68]. In addition, the optical path lengths and point spread functions of different scan fields would also increase the differences in detection signal sensitivity as the beam is scanned laterally. Furthermore, faster camera speeds can also lead to lower imaging intensity sensitivity due to the decrease in data acquisition time, requiring higher incident power [69].

We have demonstrated common-path OCE, in which M-mode phase stability evaluation (Section 3) and M-mode surface displacement detection (Section 4) were performed. Only the repeated A-scan acquisitions of the same lateral location (no scan), the same imaging depth (surface), and the same camera speed (66.7 kHz) were tested. Use of this common-path design for line scan geometries or volumetric measurements will require further evaluation to demonstrate uniform phase stability at different scanning depths and locations.

## Conclusions

We have demonstrated common-path PhS-OCE and compared it with conventional PhS-OCE. A low dominant frequency (~21 Hz) dynamic turbulence was observed in our lab environment with both techniques. The common-path technique effectively reduced the amplitude of background dynamic displacement noise from a micrometer level in conventional PhS-OCE to a sub-nanometer level in common-path PhS-OCE. Common-path PhS-OCE enables a more stable phase baseline from which to measure sample displacement, a larger dynamic detection range, and higher detection sensitivity in surface displacement measurements than conventional PhS-OCE.

## Funding

NIH/NEI R01-EY022362, P30EY07551 and P30EY003039.

## Acknowledgment

We thank Dr. Jason Marsack for assistance with manufacturing of optical plates; Alexander Zotov for valuable control software modifications. We also thank Dr. Boyu Gu, Dr. Yuqiang Bai, and Dr. Jing Lu for helpful discussion.

## Disclosures

GL: (P), MS: (P), KL: (P), MDT: (P)